

Equivalent Model of Electric Vehicles with Fast Chargers for Static and Dynamic Grid Studies

Davide del Giudice, *Member, IEEE*, Angelo Maurizio Brambilla, *Member, IEEE*, Federico Bizzarri, *Senior Member, IEEE*, Daniele Linaro, *Member, IEEE*, and Samuele Grillo, *Senior Member, IEEE*

Abstract—The growing deployment of electric mobility calls for static and dynamic grid studies to investigate to which extent it affects the grid operation and how to validate the countermeasures. Detailed electric vehicle (EV) models, which allow analyzing electrical variables at the EV charger and battery levels, are inadequate for this purpose, as they can have an excessive complexity and are computationally burdensome for large-scale grid studies. To address this issue, we exploit a detailed EV model using an analytical approach, and develop an equivalent model of EVs with fast chargers that is easy to implement and computationally efficient, while retaining adequate accuracy. Simulation results of distribution and transmission systems, modified by adding fleets of EVs, are used to demonstrate the compatibility of the proposed model for static and dynamic grid studies, even when different cathode chemistries and charging strategies are adopted.

Index Terms—Electric vehicle (EV), electric mobility, fast charger, equivalent model, distribution system, transmission system, power system simulation, small-signal model.

I. INTRODUCTION

ELECTRIC mobility has grown significantly in the past few years, leading to a global fleet of over 25 million electric vehicles (EVs) in 2023 [1]. However, the rising popularity of EVs challenges modern power systems, because it induces larger voltage drops and losses as potential adverse effects of grid overloads [2]. A vast literature was produced to analyze these phenomena and develop countermeasures such as delayed or controlled charging strategies, which postpone or minimize the need for grid reinforcements [3]. While the effectiveness of these strategies was studied at

considerable length [4], [5], relatively little attention has been paid to the derivation of static and dynamic reduced-order EV models, which are essential to accurately and quickly assess the impact of electric mobility on the grid. Detailed EV models, which allow analyzing electrical variables at EV charger and battery levels, are inadequate for this purpose, as they lead to prohibitive central processing unit (CPU) time and an excessive degree of accuracy for large-scale grid studies.

Reduced-order load models can be grouped into three categories: statistical, artificial intelligence (AI)-based, and deterministic [6]. The main issue in developing models that belong to the former two categories is that a large amount of data from different EV chargers are needed. For example, in the case of statistical models, such data are used to build probability density functions that describe the EV charging time, location, duration, and initial state of charge (SoC). Unless open datasets such as those in [7] are used, gathering this information may be complicated and time-consuming. On the contrary, deterministic models, which are the focus of this paper, are easier to develop since they are usually derived by simulating or observing small-scale systems (e.g., a single EV charger). These models can be static or dynamic and consist of simple mathematical representations that relate the EV charging power and voltage.

Concerning static models, several works describe EVs as devices more complex than constant PQ loads (i.e., the prevalent model in the literature). Through a measurement-based approach, [8]-[10] represent EVs with a ZIP model. Other works resort to a multi-stage ZIP model, where the EV power exchange is described with piecewise functions. Each interval is defined by different ZIP model parameters and represents a given EV working condition (e.g., charging time [11] or SoC [12]). Lastly, [13] employs an exponential model, which is extended to the multi-stage version in [14]. The derivation of each model hinges on a measurement-based approach, which consists of simulating or recording voltage disturbances at the EV point of connection and tuning the model parameters to fit the EV power exchange.

The models described so far are exclusively adequate for static grid studies (e.g., power flow (PF)), but not for dynamic ones (e.g., time-domain simulations), as they mirror the behavior of EVs only at steady state instead of during the regular EV charging process or after disturbances. For this

Manuscript received: November 6, 2024; revised: April 5, 2025; accepted: June 27, 2025. Date of CrossCheck: June 27, 2025. Date of online publication: July 28, 2025.

This work was supported by the EU fund Next Generation EU (CUP D43C22003090001 PNRR NEST Spoke 6), the EU fund Next Generation EU (CUP D53D23001650006 MUR PRIN SCooPS), and the European Union's Horizon Europe Research and Innovation Programme (No. 101160665 - AHEAD project).

This article is distributed under the terms of the Creative Commons Attribution 4.0 International License (<http://creativecommons.org/licenses/by/4.0/>).

D. del Giudice (corresponding author), A. M. Brambilla, F. Bizzarri, D. Linaro, and S. Grillo are with Politecnico di Milano, Milano 20133, Italy (e-mail: davide.delgiudice@polimi.it; angelo.brambilla@polimi.it; federico.bizzarri@polimi.it; daniele.linaro@polimi.it; samuele.grillo@polimi.it).

DOI: 10.35833/MPCE.2024.001204



latter instance, dynamic models are needed. However, the literature on such models is limited. Reference [15] presents a stability analysis of a simple grid with an EV by analytically developing its small-signal model, which, however, is too complex and with too many state variables to be efficiently used in large-scale grid simulations. Dynamic models are developed in [16] and [17] through a measurement-based approach, where the transient EV power after a voltage disturbance is fitted by a first- or higher-order dynamic response. In this approach, the fitted response depends on the operating point of the system and the EV internal variables (e.g., SoC): if one of them changes, the fitted response may differ from the true value. Another missing feature of all these

models is that they do not mirror the evolutions in SoC and power during the charging process. The main features and limitations of the most relevant deterministic EV models in the literature are summarized, and the comparison results are given in Table I, where “NS”, “MEA-B”, and “MOD-B” represent “not specified”, “measurement-based”, and “model-based” (i.e., analytical), respectively; CCCV and CPCV represent constant current constant voltage and constant power constant voltage charging strategies, respectively; and LPF, LMO, NMC, and NCA represent lithium iron phosphate, lithium manganese oxide, nickel manganese cobalt oxide, and nickel cobalt aluminum oxide cathode chemistries, respectively.

TABLE I
COMPARISON RESULTS AMONG STATIC AND DYNAMIC MODELS AND PROPOSED MODEL IN THIS PAPER

Reference	Description: how is EV power exchange P_{EV} modelled? If SoC evolution is considered, how is it modelled?	Type	Charging strategy used	Cathode chemistry used	Compatibility with static grid studies (e.g., PF)	Compatibility with dynamic grid studies (e.g., time-domain simulations)	
						Is EV behavior after disturbances replicated?	Is SoC updated during EV charging process?
[8], [10]	P_{EV} is modelled as a ZIP load, whose parameters do not change with SoC	MEA-B	CCCV	NS	√	×	×
[9]	P_{EV} is modelled as different modified ZIP loads, whose power exchange depends on current rather than voltage. Regardless of load model used, its parameters do not vary with SoC	MEA-B	CCCV	NS	√	×	×
[11]	P_{EV} is modelled as a multi-stage ZIP load, whose parameters change with charging time	MEA-B	NS	NS	√	×	×
[12]	P_{EV} is modelled as a multi-stage load, whose parameters change with SoC	MEA-B	NS	NS	√	×	×
[13]	P_{EV} is modelled as an exponential load, whose parameters do not change with SoC	MEA-B	NS	NS	√	×	×
[14]	P_{EV} is modelled as a multi-stage ZIP/exponential load, whose parameters change with SoC	MEA-B	CCCV	NS	√	×	×
[15]	P_{EV} variations following disturbances are described through a small-signal model	MOD-B	NS	NS	×	√	×
[16]	P_{EV} at steady state is modelled as a multi-stage ZIP/exponential load, whose parameters change with SoC. Changes in P_{EV} after disturbances are mirrored by an additional exponential recovery load model that synthesizes only first-order responses (i.e., exponentials)	MEA-B	CCCV	NS	×	√ (only if behavior is exponential)	×
[17]	P_{EV} is described with a dynamic load model based on the vector fitting technique, which can synthesize responses of any order through a frequency-dependent block	MEA-B	CCCV	NS	√	√	×
This paper	P_{EV} at steady state and SoC are described by compact representations that can consider different cathode chemistries and methods. Changes in P_{EV} after disturbances are mirrored by a couple of transfer functions that can also synthesize oscillatory responses	MOD-B	CCCV, CPCV	LFP, LMO, NMC, NCA	√	√	√

In this paper, we propose an equivalent model of EVs with fast chargers, which is easy to implement, accurate, computationally efficient, and compatible with static and dynamic grid studies. The proposed model is derived using an analytical approach by considering a detailed EV model and exploiting the fact that fast charging stations usually need one hour or more to charge a vehicle. Thus, the SoC and other battery-related variables can be deemed slow-varying, and, as such, given by a predominant low-frequency compo-

nent. Hence, their high-frequency components can be safely neglected to obtain a simpler yet accurate equivalent model.

The key features of the proposed model are described as follows.

1) The proposed model mirrors the dependence of EV power exchange on the SoC, voltage, charging strategy (i.e., CPCV and CCCV), and cathode chemistry. This latter aspect is novel since previous works in Table I typically considered Li-ion batteries without specifying the cathode chemistry.

However, this feature is important in static grid studies. Indeed, in some cases, the power absorbed by EV at a given SoC changes with the cathode chemistry. In the grids with a significant share of EVs, disregarding this aspect (e.g., by replacing EVs with only constant PQ loads) would lead to an incorrect estimation of the true grid overload and losses induced by EVs. In this paper, we select the most popular cathode chemistries available today on the EV market [18], [19]: LFP, LMO, NMC, and NCA.

2) Contrary to other models in Table I, the proposed model replicates how both the SoC and power exchange evolve during regular EV charging process and after disturbances.

II. EVS IN A NUTSHELL

Developing an equivalent model of EVs with fast chargers requires executing three preliminary steps: ① identifying the EV components that are most relevant, ② defining the EV charging control scheme, and ③ selecting realistic components and control parameters.

A. EV Components

When parked for charging, the most relevant elements of EVs are the battery pack and charger. Figure 1(a) depicts an implementation example, where the EV charger includes a two-stage AC/DC converter and DC/DC converter [8], while the battery comprises N_{cell} parallel branches of N_{cell} series-connected cells. v_{AC} is the AC-side voltage of the converter. The specific EV model that we are trying to reduce is given by the blocks in Fig. 1. Hereafter, variables with “~” notation are in per unit (p.u.), those with subscript “ref” are the reference values, and those with subscript “PF” refer to the PF (i.e., the steady-state solution).

In Fig. 1(b), the AC side of the AC/DC converter is described by a single-phase schematic, which includes an R_F - L_F filter and an e_r - e_i dependent voltage source, where R_F and L_F are the resistance and inductance of the filter, respectively; and e_r and e_i are the real and imaginary parts of the dependent voltage, respectively. As in PowerFactory, we assume voltages/currents of the external grid to be formulated in the global synchronous reference frame and given by a real component r and imaginary component i [20]. A phase locked loop (PLL) synchronizes this frame with the dq one, which is internal to the converter. The DC side of the AC/DC converter is given by a capacitor C_{DC_1} and a dependent current source i_{conv} acting as an ideal active power coupler by enforcing $e_r i_r + e_i i_i = v_{\text{DC}} i_{\text{conv}}$, where v_{DC} is the DC-side voltage of the converter, at which the capacitor C_{DC_1} operates; and i_r and i_i are the real and imaginary parts of the current at the point of connection of the EV charger, respectively. The dependent sources δi_{DC} and δv_{DC} , together with the L_{DC} - C_{DC_2} filter, implement the lossless average model of the DC/DC converter described in [21]. Lastly, a dependent voltage source mirrors the voltage due to the series connection of N_{cell} cells. Note that in Fig. 1(b), Q_{EV} is the reactive power absorbed by the electric vehicle charger; P_{conv} and Q_{conv} are the active power and reactive power absorbed by the AC/DC converter, which basically correspond to P_{EV} and Q_{EV} minus the losses inside the converter, respectively; P_{batt} is the

power absorbed by the battery; i_{batt} is the current absorbed by the battery; v_{batt} is the battery voltage; v_{cell} is the voltage of one of the cells that make up the battery; i_{DC} is the current absorbed by the DC/DC converter; P_{DC} is the power absorbed by the DC/DC converter; v_r and v_i are the real and imaginary parts of the voltage at the point of connection of the EV charger, respectively.

Figure 1(c) depicts the schematic of a single battery cell. The dependent current source relates the cell and battery currents i_{cell} and i_{batt} through the number of parallel branches N_{cell} . The single cell can be described through models of different degrees of accuracy [22]. Here we represent it with an equivalent resistance R_{cell} and a dependent voltage source that imposes the open circuit voltage (OCV) v_{OCV} . As shown in Fig. 1(d), this voltage depends on the SoC of battery cell through a non-linear relationship $f(\cdot)$. In turn, the SoC evolves as $\frac{d\text{SoC}}{dt} = \frac{i_{\text{cell}}}{3600Q_{\text{cell}}}$, where Q_{cell} is the nominal capacity. Indeed, SoC is the ratio between the charged energy stored in the battery cell (i.e., the integral of i_{cell} over time) and the maximum capacity, related to the nominal value Q_{cell} . This expression, referred to as Coulomb counting, includes the constant 3600 at the denominator since i_{cell} is in Ampere, Q_{cell} is in Ah, and the elapsed time is in second.

In this paper, we select the v_{OCV} -SoC relationship of the cathode chemistries depicted in Fig. 1(e), obtained from the experimental results reported in [23].

B. EV Charging Control Scheme

The two conversion stages in the EV charger have distinct roles. By exploiting variables in the dq frame [24], the AC/DC converter control in Fig. 1(f) keeps the voltage v_{DC} across the capacitor C_{DC_1} at $v_{\text{DC}}^{\text{ref}}$ and no reactive power of EV Q_{EV} is exchanged (i.e., $\tilde{Q}^{\text{ref}}=0$). These controls (i.e., outer loop) define a reference value for the currents \tilde{i}_d and \tilde{i}_q , translated by an inner current loop into the \tilde{e}_r and \tilde{e}_i components of the dependent voltage source. To implement these controls, a PLL is used, which synchronizes the internal reference frame (i.e., dq frame) with the external one by deriving the value of the angular frequency of the system ω . In Fig. 1(f), \tilde{v}_d , \tilde{v}_q , \tilde{i}_d , and \tilde{i}_q are the counterparts of \tilde{v}_r , \tilde{v}_i , \tilde{i}_r , and \tilde{i}_i in the dq frame, respectively.

The control scheme of the DC/DC converter, as shown in Fig. 1(g), regulates the duty cycle δ so that the power absorbed by the battery pack matches the reference value P^{ref} . This value is defined based on the pseudo-code in Fig. 1(g), which considers two main charging strategies: CPCV or CCCV [22].

In both strategies, the cell voltage v_{cell} is compared with a threshold value v_{th} . If v_{cell} is lower than v_{th} , the converter control works in the constant power (CP) or constant current (CC) segment if CPCV or CCCV charging strategy is adopted, respectively. Otherwise, it works in the constant voltage (CV) segment. In Fig. 1(g), the segment considered at a specific time step is denoted by the flag variables CP , CC , and CV . As specified by the pseudo-code, only one variable at a time can be 1, while the others are 0. Based on the segment considered, the DC/DC converter control scheme regulates either the battery power P_{batt} , current i_{batt} , or voltage v_{batt} to track a reference value given by the superscript “ref”. In

turn, as shown in Fig. 1(g), $i_{\text{batt}}^{\text{ref}}$, $P_{\text{batt}}^{\text{ref}}$ and $v_{\text{cell}}^{\text{ref}}$ determine P^{ref} through a proportional-integral (PI) controller.

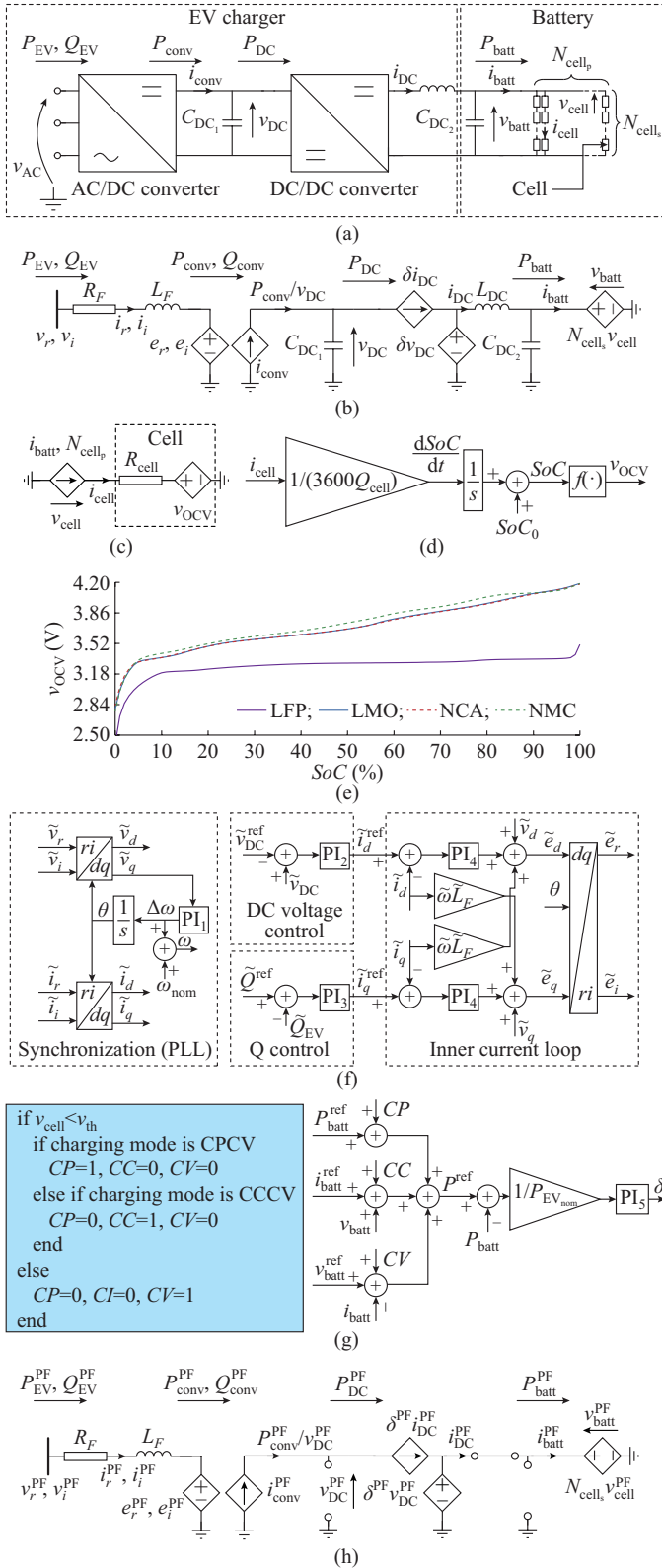


Fig. 1. Schematic of EV components. (a) Implementation example of EV charger and battery. (b) Schematic of AC/DC and DC/DC converters. (c) Schematic of a single battery cell. (d) $i_{\text{cell}}-v_{\text{OCV}}$ relationship of a single cell. (e) $v_{\text{OCV}}-SoC$ relationship of cathode chemistries. (f) EV charging control scheme. (g) Control scheme of DC/DC converter. (h) Schematic of converters at steady state.

C. Realistic Components and Control Parameters

The proposed model in this paper stems from real EVs with fast chargers. We choose a fast charger with nominal power $P_{\text{EV, nom}} = 50$ kW (a value compatible with [2]), and nominal AC and DC voltages $v_{\text{AC, nom}} = 400$ V and $v_{\text{DC, nom}} = 800$ V, respectively. The 2017 Tesla Model S is picked as reference EV with a battery capacity $E_{\text{EV, nom}} = 75$ kWh [25] and a nominal battery voltage $v_{\text{batt, nom}} = 400$ V. The other parameters in Table II are used to describe each cathode chemistry employed in the EV battery pack, converter, and PI controller. Note that $k_{p1}-k_{p5}$ and $k_{i1}-k_{i5}$ are the proportional and integral gains of the PI controllers PI₁-PI₅, respectively

TABLE II
PARAMETERS OF EV WITH FAST CHARGER

Type	Parameter	Cathode chemistry	Value
Battery cell parameters	$v_{\text{cell, nom}}$ (V)	LFP	3.2
		LMO	3.7
		NCA	3.6
		NMC	3.6
		LFP	2.6
	Q_{cell} (Ah)	LMO	2.6
		NCA	3.0
		NMC	2.0
		LFP	0.080
		LMO	0.087
R_{cell} (Ω)	NCA	0.088	
	NMC	0.060	
	LFP	3.488	
	LMO	4.188	
	NCA	4.188	
Charging station parameters	NMC	4.183	
	R_F (m Ω)	-	3.20
	L_F (mH)	-	0.2
	$C_{\text{DC}1}$ (mF)	-	25
	L_{DC} (mH)	-	0.1
Control reference values	$C_{\text{DC}2}$ (mF)	-	0.5
	$v_{\text{DC}}^{\text{ref}}$ (V)	-	800
	Q^{ref} (var)	-	0
	$P_{\text{batt}}^{\text{ref}}$ (kW)	-	$P_{\text{EV, nom}}$
	$v_{\text{batt}}^{\text{ref}}$ (V)	-	$N_{\text{cell}} v_{\text{th}}$
PI controller parameters	$i_{\text{batt}}^{\text{ref}}$ (A)	-	$P_{\text{batt}}^{\text{ref}}/v_{\text{batt, nom}}$
	k_{p1}, k_{i1}	-	490, 122500
	k_{p2}, k_{i2}	-	0.6, 1
	k_{p3}, k_{i3}	-	100, 1000
	k_{p4}, k_{i4}	-	0.142, 44
	k_{p5}, k_{i5}	-	1000, 0.1

III. PROPOSED EQUIVALENT MODEL OF EVs WITH FAST CHARGERS

Figure 2 depicts the proposed equivalent model of EVs. It uses the components of the EV voltage v_r, v_i at its point of connection and its initial state of charge SoC_0 as inputs, while it provides the SoC and active power exchange P_{EV}

over time as outputs ($Q_{EV}=0$ as enforced by the EV power control). In Fig. 2, the LPF label denotes a low-pass filter; the notation $\angle(\cdot)$ denotes the phase; and \mathcal{L} and \mathcal{L}^{-1} denote the direct and inverse Laplace transforms, respectively.

These transforms exist just for mathematical rigor: during simulation, the operations in block ⑥ are actually carried out by solving a linear time-variant system of ordinary differential equations. The coefficients in blocks ② and ③ will be defined in the equations in the following text.

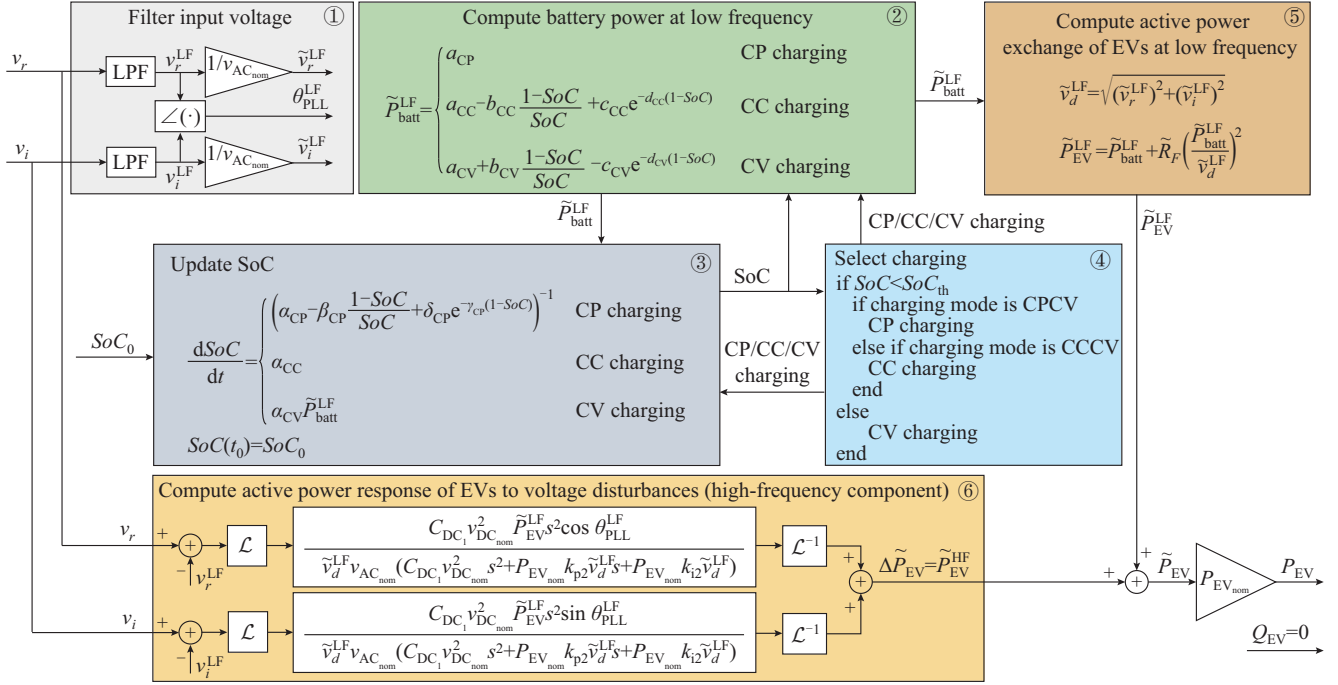


Fig. 2. Proposed equivalent model of EVs with fast chargers.

Assume that a generic variable x can be seen as a sum of a low-frequency component x^{LF} and high-frequency component x^{HF} , indicated by superscripts LF and HF, respectively. The proposed model relies on the observation that some variables in the EV are characterized by a predominant low-frequency component. For instance, the EV selected in this paper requires $E_{EV, nom}/P_{EV, nom} \approx 1.5$ hours for a full charge. Hence, its SoC is a relatively slow-varying quantity, and thus, $SoC \approx SoC^{LF}$ (and the same holds for other battery-related variables). On the contrary, the active power exchange of EVs includes both components, so that $P_{EV} = P_{EV}^{LF} + P_{EV}^{HF}$. P_{EV}^{LF} mirrors the power exchange due to the regular EV charging, while P_{EV}^{HF} is linked to the EV power response to voltage disturbances, which usually lasts for less than a minute based on the control parameters used.

Figure 2 includes several blocks. Through the voltages v_r and v_i and the LPFs, block ① derives their low-frequency components \tilde{v}_r^{LF} and \tilde{v}_i^{LF} (and their p.u. counterparts \tilde{v}_r^{LF} and \tilde{v}_i^{LF}), as well as the angle θ_{PLL}^{LF} that would be provided by the PLL. The cut-off frequency of the LPF f_c is set to be 0.1 Hz. This tuning, detailed in Supplementary Material A, grants the high accuracy of the proposed model in dynamic grid studies. The low-frequency component of power exchange of battery pack \tilde{P}_{batt}^{LF} is calculated in block ②, while block ③ updates the SoC over time starting from its initial value SoC_0 . Both blocks include expressions that depend on SoC, as well as the charging mode (i.e., CP/CC/CV). At each time step, block ④ selects the charging mode to be considered by comparing the SoC with a threshold value SoC_{th} and know-

ing if the EV employs either CPCV or CCCV charging strategy, thus mirroring the pseudo-code of Fig. 1(g). Block ⑤ computes \tilde{P}_{EV}^{LF} , while in block ⑥, two transfer functions are used to translate any change in EV voltage with respect to \tilde{v}_r^{LF} and \tilde{v}_i^{LF} into an active power variation $\Delta\tilde{P}_{EV}$, which corresponds to the high-frequency component of active power \tilde{P}_{EV}^{HF} . This variable is summed to \tilde{P}_{EV}^{LF} and multiplied by $P_{EV, nom}$ to obtain the total power exchange P_{EV} at any time instant.

So far, the proposed equivalent model of EVs is described only at high level. The next subsections detail how the equations and parameters inside the blocks in Fig. 2 can be derived.

A. Equivalent Model Behavior at Steady State

If static grid studies are executed, $SoC = SoC_0$, $\Delta\tilde{P}_{EV} = 0$, and the LPFs in block ① of Fig. 2 are inconsequential, as the input and output are identical in the PF analyses. Thus, variables with superscripts “PF” and “LF” convey the same information only at steady state. The underlying approximation put forward in the equivalent model in Fig. 2 is that the equivalence between these two sets of variables persists in the whole low-frequency range. This approximation does not affect the accuracy of the proposed model, which will be shown in Section IV.

The voltages \tilde{v}_d and \tilde{v}_q in Fig. 1(f) depend on v_r and v_i :

$$\begin{cases} \tilde{v}_d = (v_r \cos \theta_{PLL} + v_i \sin \theta_{PLL}) \frac{1}{v_{AC, nom}} \\ \tilde{v}_q = (-v_r \sin \theta_{PLL} + v_i \cos \theta_{PLL}) \frac{1}{v_{AC, nom}} \end{cases} \quad (1)$$

This transformation is power-invariant. Thus, we have:

$$\begin{cases} \tilde{P}_{EV} = \tilde{v}_r \tilde{i}_r + \tilde{v}_d \tilde{i}_d = \tilde{v}_d \tilde{i}_q + \tilde{v}_q \tilde{i}_q \\ \tilde{Q}_{EV} = -\tilde{v}_r \tilde{i}_i + \tilde{v}_i \tilde{i}_r = -\tilde{v}_d \tilde{i}_q + \tilde{v}_q \tilde{i}_d \end{cases} \quad (2)$$

When the PF solution is found, the input of each PI controller in Fig. 1(f) and (g) is zero, and the schematic of converters becomes the one in Fig. 1(h). These two features allow us to derive:

$$\begin{cases} \tilde{v}_q^{LF} = 0 \\ \theta_{PLL}^{LF} = \tan \theta_{PLL}^{LF} = v_i^{LF}/v_r^{LF} \\ \tilde{v}_d^{LF} = \frac{v_r^{LF} \cos \theta_{PLL}^{LF} + v_i^{LF} \sin \theta_{PLL}^{LF}}{v_{AC, nom}} = \frac{\sqrt{(v_r^{LF})^2 + (v_i^{LF})^2}}{v_{AC, nom}} \\ \tilde{v}_{DC}^{LF} = \tilde{v}_{DC}^{ref} = \frac{v_{DC, nom}}{v_{DC, nom}} = 1 \\ \tilde{Q}_{EV}^{LF} = \tilde{Q}_{EV}^{ref} = 0 \\ \tilde{P}_{EV}^{LF} = \tilde{v}_d^{LF} \tilde{i}_d^{LF} + \tilde{v}_q^{LF} \tilde{i}_q^{LF} \\ \tilde{i}_q^{LF} = -\frac{\tilde{Q}_{EV}^{LF} - \tilde{v}_q^{LF} \tilde{i}_d^{LF}}{\tilde{v}_d^{LF}} = 0 \\ \tilde{P}_{conv}^{LF} = \tilde{e}_d^{LF} \tilde{i}_d^{LF} + \tilde{e}_q^{LF} \tilde{i}_q^{LF} = \tilde{P}_{batt}^{LF} \end{cases} \quad (3)$$

Considering these properties and Fig. 1(h), the active power exchange \tilde{P}_{EV}^{LF} can be rewritten as:

$$\begin{aligned} \tilde{P}_{EV}^{LF} &= \tilde{v}_d^{LF} \tilde{i}_d^{LF} = (\tilde{e}_d^{LF} + \tilde{R}_F \tilde{i}_d^{LF}) \tilde{i}_d^{LF} = \\ &\tilde{P}_{batt}^{LF} + \tilde{R}_F (\tilde{i}_d^{LF})^2 \approx \tilde{P}_{batt}^{LF} + \tilde{R}_F \left(\frac{\tilde{P}_{batt}^{LF}}{\tilde{v}_d^{LF}} \right)^2 \end{aligned} \quad (4)$$

where the last approximation is performed assuming that the filter resistance \tilde{R}_F is small enough so that the voltage drop across it can be negligible, and $\tilde{i}_d^{LF} \approx \tilde{P}_{batt}^{LF} / \tilde{v}_d^{LF}$.

Expanding (4) requires finding a formula of the power absorbed by the battery pack $P_{batt}^{LF} = v_{batt}^{LF} i_{batt}^{LF}$. This value mainly depends on two factors: the SoC of the battery pack and the charging mode (i.e., CP, CC, and CV). As stated in Section II-B, based on the charging mode, one of P_{batt}^{LF} , i_{batt}^{LF} , and v_{batt}^{LF} equals its reference value. Considering Fig. 1(h), \tilde{P}_{batt}^{LF} can be computed in each charging mode as:

$$\tilde{P}_{batt}^{LF} = \begin{cases} \frac{P_{batt}^{ref}}{P_{EV, nom}} & \text{CP charging} \\ \frac{R_{batt} (I_{batt}^{ref})^2 + I_{batt}^{ref} N_{cell_s} v_{OCV}(SoC)}{P_{EV, nom}} & \text{CC charging} \\ \frac{v_{batt}^{ref} (v_{batt}^{ref} - N_{cell_s} v_{OCV}(SoC))}{R_{batt} P_{EV, nom}} & \text{CV charging} \end{cases} \quad (5)$$

where $R_{batt} = R_{cell} N_{cell_s} N_{cell_p}$. Contrary to the case of CP charging, the computation of P_{batt}^{LF} with CC and CV charging requires knowing v_{OCV} over the whole range of SoC during the EV charging process. However, one has to store in a look-up table as many entries of P_{batt}^{LF} as the number of SoC values con-

sidered (as done in multi-stage EV load modeling [11]). Albeit not problematic from a computational standpoint, we follow a different approach and derive an analytical expression for P_{batt}^{LF} , which grants a more compact representation of the overall EV model. To achieve this, we fit the non-linear relationship $f(\cdot)$ between v_{OCV} and SoC in Fig. 1(e) with the model [26] as:

$$v_{OCV}(SoC) = E_0 - K \frac{1 - SoC}{SoC} Q_{cell} + A e^{(1 - SoC) B Q_{cell}} \quad (6)$$

where E_0 , K , A , and B are the cell parameters that vary with the cathode chemistry. This formulation is also used in the battery model of Simulink [27].

By using (6), (5) is specialized as (7). These equations appear in blocks ② and ③ of Fig. 2, which allow computing the steady-state active power exchange of EVs.

$$\tilde{P}_{batt}^{PF} = \begin{cases} \frac{P_{batt}^{PF}}{P_{EV, nom}} & \text{CP charging} \\ \frac{R_{batt} (I_{batt}^{ref})^2 + E_0 N_{cell_s} I_{batt}^{ref}}{P_{EV, nom}} - \frac{K Q_{cell} N_{cell_s} I_{batt}^{ref}}{P_{EV, nom}} \frac{1 - SoC}{SoC} + \frac{AN_{cell_s} I_{batt}^{ref}}{P_{EV, nom}} e^{-Q_{cell} B (1 - SoC)} & \text{CC charging} \\ \frac{v_{batt}^{ref} (v_{batt}^{ref} - E_0 N_{cell_s})}{R_{batt} P_{EV, nom}} - \frac{K Q_{cell} v_{batt}^{ref} N_{cell_s}}{R_{batt} P_{EV, nom}} \frac{1 - SoC}{SoC} + \frac{Av_{batt}^{ref} N_{cell_s}}{R_{batt} P_{EV, nom}} e^{-Q_{cell} B (1 - SoC)} & \text{CV charging} \end{cases} \quad (7)$$

In the next subsections, we show how the proposed model also captures the following concerns: ① how the SoC evolves over time through charging, and ② how the active power exchange of EVs varies after a voltage disturbance occurs at terminals.

B. SoC Update of Equivalent EV Model

Based on Fig. 1(d), the derivative of SoC during the charging process is expressed by:

$$\frac{dSoC}{dt} = \frac{1}{3600 Q_{cell}} i_{cell} = \frac{1}{3600 Q_{cell} N_{cell_p}} i_{batt} \quad (8)$$

The expansion of this formula requires determining how i_{batt} differs in each charging mode. Considering again how each of them operates, i_{batt} can be computed as:

$$i_{batt} \approx i_{batt}^{LF} \approx i_{batt}^{ref} \approx \begin{cases} \varepsilon \frac{P_{batt}^{ref}}{N_{cell_s} v_{OCV} \cdot SoC} & \text{CP charging} \\ i_{batt}^{ref} & \text{CC charging} \\ \frac{\tilde{P}_{batt}^{LF} P_{EV, nom}}{v_{batt}^{ref}} & \text{CV charging} \end{cases} \quad (9)$$

where ε is a correction factor. Such formulas are approximations for two reasons. First, one assumption common to all

charging modes is that each variable of the battery is assumed to track perfectly its reference counterpart (e.g., $i_{\text{batt}} = i_{\text{batt}}^{\text{ref}}$ with CC charging). Although this is true for steady-state operating conditions, it may not be exact during time-domain simulations, where disturbances such as voltage variations at the point of connection of EV may be analyzed. However, as already stated, EV charging is a relatively slow process compared with its power response after a disturbance. Thus, during a short disturbance, one can assume that the SoC will not deviate significantly from its pre-disturbance value, which is captured by its low-frequency component. The same also holds true for all the other battery-related variables including i_{batt} , and hence $i_{\text{batt}} \approx i_{\text{batt}}^{\text{LF}} \approx i_{\text{batt}}^{\text{ref}}$ in (9). Concerning the CP charging, i_{batt} is computed by neglecting the voltage drop across the battery resistance R_{batt} , so that $i_{\text{batt}} = \frac{P_{\text{batt}}^{\text{ref}}}{v_{\text{batt}}} \approx \frac{P_{\text{batt}}^{\text{ref}}}{N_{\text{cell}_s} v_{\text{OCV}} \cdot \text{SoC}}$. On one hand, this assumption

grants a compact expression of $\frac{d\text{SoC}}{dt}$ during CP charging, but on the other hand, it leads to a loss in accuracy. To address this issue, (9) includes a correction factor ε , which is heuristically set to be 0.97 with a fitting process aimed at minimizing the difference between the derivative of SoC in the proposed model.

Through (6) and (9), (8) can be recast as:

$$\frac{d\text{SoC}}{dt} = \left\{ \begin{array}{l} \underbrace{\frac{3600Q_{\text{cell}} N_{\text{cell}_p} N_{\text{cell}_s} E_0}{\varepsilon P_{\text{batt}}^{\text{ref}}} - \frac{3600Q_{\text{cell}}^2 N_{\text{cell}_p} N_{\text{cell}_s} K}{\varepsilon P_{\text{batt}}^{\text{ref}}}}_{\alpha_{\text{CP}}} \\ \frac{1 - \text{SoC}}{\text{SoC}} + \frac{3600A N_{\text{cell}_p} N_{\text{cell}_s}}{\varepsilon P_{\text{batt}}^{\text{ref}}} e^{-\frac{\gamma_{\text{CP}}}{Q_{\text{cell}} B} (1 - \text{SoC})} \\ \underbrace{\frac{I_{\text{batt}}^{\text{ref}}}{3600Q_{\text{cell}} N_{\text{cell}_p}}}_{\alpha_{\text{CC}}} \\ \underbrace{\frac{P_{\text{EV, nom}}}{3600v_{\text{batt}}^{\text{ref}} Q_{\text{cell}} N_{\text{cell}_p}}}_{\alpha_{\text{CV}}} P_{\text{batt}}^{\text{LF}} \end{array} \right\} \text{CP charging} \quad \text{CC charging} \quad \text{CV charging} \quad (10)$$

C. Active Power Response of Equivalent EV Model

We now show how to derive the transfer functions of block ⑥ in Fig. 3, which mirror how the active power exchange of EV varies after a voltage disturbance at its point of connection. This derivation is based on the following three assumptions described as follows.

1) The inner current control loop has an infinite bandwidth (i.e., the inner current loop is so fast that $i_d^{\text{ref}} \approx i_d$ and $i_q^{\text{ref}} \approx i_q$; thus, we have their small-signal variations $\Delta i_d^{\text{ref}} \approx \Delta i_d$ and $\Delta i_q^{\text{ref}} \approx \Delta i_q$). Indeed, PI control parameters of the inner control loop are often tuned so that their cut-off frequency is at least one decade higher than that of the outer loop.

2) During the response to a voltage disturbance, the SoC

of EV batteries can be considered constant (equal to its pre-disturbance value) because the EV charging is a relatively slow process.

3) Regarding the parameters of DC/DC converter control, P_{DC} in Fig. 1(b) is almost constant right after a disturbance and equal to $P_{\text{batt}}^{\text{LF}}$. Its corresponding small-signal variation is thus zero. $P_{\text{DC}}^{\text{LF}}$ can also be computed as $P_{\text{batt}}^{\text{LF}} = P_{\text{EV, nom}} \left(\tilde{P}_{\text{EV}}^{\text{LF}} - \tilde{R}_F (\tilde{i}_d^{\text{LF}})^2 \right)$, where \tilde{R}_F is the per unit value of the filter resistance in Fig. 1(b); and \tilde{i}_d^{LF} is the low-frequency per unit counterpart of d -axis current flowing through the AC/DC converter.

The small-signal model of EVs can be written as:

$$\Delta \theta_{\text{PLL}} = (k_{p1} + k_{i1}s) \Delta \tilde{v}_q s \quad (11a)$$

$$\Delta \tilde{i}_d \approx \Delta \tilde{i}_d^{\text{ref}} = -(k_{p2} + k_{i2}s) \Delta v_{\text{DC}} v_{\text{DC}}^{\text{LF}} \quad (11b)$$

$$\Delta \tilde{i}_q \approx \Delta \tilde{i}_q^{\text{ref}} = (k_{p3} + k_{i3}s) \Delta \tilde{Q}_{\text{EV}} \quad (11c)$$

$$\Delta \tilde{v}_d = \frac{\Delta v_r \cos \theta_{\text{PLL}}^{\text{LF}} + \Delta v_i \sin \theta_{\text{PLL}}^{\text{LF}}}{v_{\text{AC, nom}}} - \frac{(v_r^{\text{LF}} \sin \theta_{\text{PLL}}^{\text{LF}} - v_i^{\text{LF}} \cos \theta_{\text{PLL}}^{\text{LF}})}{v_{\text{AC, nom}}} \Delta \theta_{\text{PLL}} \quad (11d)$$

$$\Delta \tilde{v}_q = \frac{-\Delta v_r \sin \theta_{\text{PLL}}^{\text{LF}} + \Delta v_i \cos \theta_{\text{PLL}}^{\text{LF}}}{v_{\text{AC, nom}}} - \frac{(v_r^{\text{LF}} \cos \theta_{\text{PLL}}^{\text{LF}} + v_i^{\text{LF}} \sin \theta_{\text{PLL}}^{\text{LF}})}{v_{\text{AC, nom}}} \Delta \theta_{\text{PLL}} \quad (11e)$$

$$\Delta \tilde{P}_{\text{EV}} = \tilde{v}_d^{\text{LF}} \Delta \tilde{i}_d + \tilde{i}_d^{\text{LF}} \Delta \tilde{v}_d + \tilde{v}_q^{\text{LF}} \Delta \tilde{i}_q + \tilde{i}_q^{\text{LF}} \Delta \tilde{v}_q \quad (11f)$$

$$\Delta \tilde{Q}_{\text{EV}} = \tilde{v}_q^{\text{LF}} \Delta \tilde{i}_d + \tilde{i}_d^{\text{LF}} \Delta \tilde{v}_q + \tilde{v}_d^{\text{LF}} \Delta \tilde{i}_q + \tilde{i}_q^{\text{LF}} \Delta \tilde{v}_d \quad (11g)$$

$$\Delta P_{\text{conv}} = P_{\text{EV, nom}} \left(\Delta \tilde{P}_{\text{EV}} - 2\tilde{R}_F \tilde{i}_d^{\text{LF}} \Delta \tilde{i}_d - 2\tilde{R}_F \tilde{i}_q^{\text{LF}} \Delta \tilde{i}_q \right) \quad (11h)$$

$$\Delta i_{\text{conv}} = \frac{\Delta P_{\text{conv}}}{v_{\text{DC}}^{\text{LF}}} - \frac{P_{\text{conv}}}{(v_{\text{DC}}^{\text{LF}})^2} \Delta v_{\text{DC}} \quad (11i)$$

$$\Delta i_{\text{conv}} = sC_{\text{DC}_1} \Delta v_{\text{DC}} + \frac{\Delta P_{\text{DC}}}{v_{\text{DC}}^{\text{LF}}} - \frac{P_{\text{DC}}^{\text{LF}}}{(v_{\text{DC}}^{\text{LF}})^2} \Delta v_{\text{DC}} \quad (11j)$$

$$\Delta P_{\text{DC}} = 0 \quad (11k)$$

where the small-signal variation of a generic variable x is denoted by Δx and is expressed in the Laplace domain.

Equations (11a)-(11c) are the small-signal model of the PLL, DC voltage, and reactive power control in Fig. 1(f), respectively; while (11d), (11e) and (11f), (11g) are linearizations of (1) and (2), respectively. As to (11h), (11i), they can be obtained by linearizing $P_{\text{conv}} = P_{\text{EV, nom}} (\tilde{P}_{\text{EV}} - \tilde{R}_F \tilde{i}_d^2 - \tilde{R}_F \tilde{i}_q^2)$ and $i_{\text{conv}} = P_{\text{conv}} v_{\text{DC}}$. Lastly, (11j) implements Kirchhoff's current law at the node where C_{DC_1} is connected, as shown in Fig. 1(b). The resulting small-signal equation includes P_{DC} , whose small-signal variation is assumed to be zero in (11k) as previously stated. All linearizations are carried out around the low-frequency component solution. Through (11) and the data derived at steady state in (3), the small-signal active power variation $\Delta \tilde{P}_{\text{EV}}$ to changes in voltages v_r and v_i can be computed as:

$$\Delta\tilde{P}_{EV} = \tilde{P}_{EV}^{HF} = G_r(s)\Delta v_r + G_i(s)\Delta v_i \quad (12)$$

where the expressions of $G_r(s)$ and $G_i(s)$ are given in (13), and the subscript ‘‘approx’’ represents the approximate ver-

sion. The steps to derive the expressions of $G_r(s)$ and $G_i(s)$ are not shown here as they are lengthy and of limited-added value. A Mathematica notebook that symbolically derives them is available at the GitHub repository [28].

$$G_r(s) = \frac{\overbrace{C_{DC_1} v_{DC_{nom}}^2 \tilde{P}_{EV}^{LF} \tilde{v}_d^{LF} s^2 - 2P_{EV_{nom}} \tilde{R}_F k_{p2} \left(\tilde{P}_{EV}^{LF}\right)^2 s - 2P_{EV_{nom}} \tilde{R}_F k_{i2} \left(\tilde{P}_{EV}^{LF}\right)^2}}^{\eta}}{\tilde{v}_d^{LF} v_{AC_{nom}} \left[C_{DC_1} v_{DC_{nom}}^2 \tilde{v}_d^{LF} s^2 + P_{EV_{nom}} k_{p2} \left(\tilde{v}_d^{LF}\right)^2 - 2\tilde{R}_F \tilde{P}_{EV}^{LF} \right] s + P_{EV_{nom}} k_{i2} \left(\tilde{v}_d^{LF}\right)^2 - 2\tilde{R}_F \tilde{P}_{EV}^{LF}} \cos \theta_{PLL}^{LF} \quad (13a)$$

$$G_i(s) = \eta \sin \theta_{PLL}^{LF} \quad (13b)$$

$$G_{r,approx}(s) = \lim_{\tilde{R}_F \rightarrow 0} G_r(s) = \frac{\overbrace{C_{DC_1} v_{DC_{nom}}^2 \tilde{P}_{EV}^{LF} s^2}}^{\lambda}}{\tilde{v}_d^{LF} v_{AC_{nom}} \left(C_{DC_1} v_{DC_{nom}}^2 s^2 + P_{EV_{nom}} k_{p2} \tilde{v}_d^{LF} s + P_{EV_{nom}} k_{i2} \tilde{v}_d^{LF} \right)} \cos \theta_{PLL}^{LF} \quad (13c)$$

$$G_{i,approx}(s) = \lim_{\tilde{R}_F \rightarrow 0} G_i(s) = \lambda \sin \theta_{PLL}^{PF} \quad (13d)$$

As shown in (13c) and (13d), these expressions can be further reduced by neglecting the filter resistance \tilde{R}_F , at least for the EV small-signal response, thus giving shape to the transfer functions depicted in block ⑥ of Fig. 2. As shown in the following text, this simplification has negligible impact on the accuracy.

The previously derived transfer functions deserve some further comments. To begin with, P_{EV}^{HF} depends only on the parameters of the PI regulators devoted to DC voltage control (i.e., k_{p2} and k_{i2}). This is in line with [17], which states that such parameters are those primarily responsible for the EV active power response. Moreover, the reliance on LPF in block ① of Fig. 2 is such that the dynamic response ob-

tained by block ⑥ is valid through the whole EV charging process, rather than only for working conditions close to the PF solution. This is in contrast with measurement-based models [17], which may not yield accurate results if the EV dynamic response is analyzed starting from an operating point different from where the recorded response is fitted.

By fitting the v_{OCV} - SoC curves in Fig. 1(e) with (6) (see Supplementary Material A for more details on this aspect), using the data in Table II, and exploiting (7), (10), and (13), the parameters in Tables III and IV are derived. These parameters are needed to simulate the proposed model with each cathode chemistry and charging mode.

TABLE III
BATTERY-RELATED PARAMETERS REQUIRED TO SIMULATE EVS WITH EACH CATHODE CHEMISTRY AND CHARGING MODE

Chemistry	a_{CP}	a_{CC}	$b_{CC} (10^{-3})$	c_{CC}	d_{CC}	a_{CV}	b_{CV}	c_{CV}	d_{CV}	$\alpha_{CP} (10^3)$	β_{CP}	$\delta_{CP} (10^3)$	γ_{CP}	$\alpha_{CC} (10^{-3})$	$\alpha_{CV} (10^{-3})$	SoC_{th}
LFP	1	0.98	5	0.02	6.82	8.69	19.82	8.69	8.30	5.90	27.97	0.14	6.81	0.17	0.17	0.987
LMO	1	0.74	3	0.29	0.99	1.54	-0.23	1.54	12.00	4.59	19.17	1.85	0.99	0.16	0.16	0.911
NCA	1	0.77	3	0.26	1.13	1.77	-0.40	1.77	8.54	4.90	21.86	1.74	1.13	0.16	0.16	0.901
NMC	1	-2.00	1	3.00	0.06	1.15	0.14	1.15	22.80	-13.20	8.99	19.80	0.06	0.16	0.16	0.914

TABLE IV
FAST CHARGER-RELATED PARAMETERS REQUIRED TO SIMULATE EVS WITH EACH CATHODE CHEMISTRY AND CHARGING MODE

$P_{EV_{nom}}^{EV}$ (kW)	$v_{AC_{nom}}$ (V)	$v_{DC_{nom}}$ (V)	\tilde{R}_F (p.u.)	C_{DC_1} (mF)	k_{p2} (p.u.)	k_{i2} (p.u.)
50	400	800	0.01	25	0.6	1

IV. VALIDATION OF PROPOSED MODEL

In this section, we validate the proposed model for static and dynamic grid studies. Such studies show that the proposed model, albeit relatively simple, provides results comparable to those obtained with detailed EV representations but with a lower computational burden. All the files needed to run the simulation shown hereafter are available in the same GitHub repository mentioned in Section III-C [28]. Simulations are performed on an Intel Xeon Gold-6238R-CPU @

2.20, running Linux Mint 20.1.

A. Static Grid Studies of a Fleet of EVs

First, we consider the K1 distribution feeder, a test system developed by the Electric Power Research Institute, USA, given by 1384 loads associated to residential, commercial, and light industrial customers [29]. We pick this benchmark as it represents a real feeder in the Northeastern USA. Its extension makes it a good mid-size option to test the effect of EV mobility. We modify the feeder by connecting a fleet of 28 EVs, indicated by green crosses in Supplementary Material B Fig. SB1. This addition leads to a grid overload of approximately 30%. Assuming that all EVs have the same initial state of charge SoC_0 , charging strategy, and cathode chemistry, we run a sequence of PF analyses by sweeping SoC_0 with a 1% step between 10% and 90% (i.e., a range compatible with CC or CP charging). While doing so, we use CPCV and CCCV charging strategies, and the previously cited cathode chemistries.

Moreover, we consider four different cases. In the first and second cases, we use the simulator PAN [30]-[32] and represent the EVs through the detailed EV model in Fig. 1 and the proposed one in Fig. 2, respectively. To prove the ease of implementation of the proposed model, in the third case, we replicate its static behavior by creating an “ad hoc” model in the simulator OpenDSS [33], and use it to carry out the same PF analyses. In the fourth case, we still use OpenDSS and represent EVs through constant PQ loads at nominal power $P_{EV_{nom}}$, as is customary in the literature. A description of PAN and OpenDSS simulators can be founded in Supplementary Material B.

Figure 3 depicts the simulation results of the modified feeder. For each colored trace (refer to the legend in the figure for their meaning), the diamond markers and dashed lines denote the results obtained with PAN by using the detailed EV model and the proposed model, respectively. The dots are the results of the proposed model by simulating the feeder and its EVs with OpenDSS. The numbers on the right side of Fig. 3(a) and (d) indicate the percentage variation of the results with respect to the case when EVs are replaced by constant PQ loads (gray horizontal line) whose nominal power is $P_{EV_{nom}}$.

Figure 3(a) shows the active power exchange \tilde{P}_{EV} of a single EV with respect to SoC_0 (note that although SoC_0 is swept with a 1% step, traces and markers are not shown with the same resolution for the sake of readability). With CCCV charging strategy, \tilde{P}_{EV} increases with SoC_0 . The magnitude of this trend depends on the cathode chemistry considered. Battery packs with LFP cells lead to a maximum power variation $\Delta\tilde{P}_{EV}$ (i.e., the relative difference between the markers at $SoC_0=10\%$ and $SoC_0=90\%$) of about 6%. This value is larger and amounts to approximately 18% for the other cathode chemistries, which behave alike due to the similarity of their $v_{OCV}-SoC$ curves (see Fig. 1(e)). On the contrary, with CPCV charging strategy, \tilde{P}_{EV} does not change with SoC_0 or the cathode chemistry (i.e., all traces superpose so that only one trace is visible).

The accuracy of the proposed model is better exemplified in Fig. 3(b) and (c), which are insets of Fig. 3(a) for different ranges of SoC_0 . The results show an almost perfect agreement among the lines and markers, which proves the accuracy of the proposed model. This feature is also confirmed by the maximum mean absolute percentage error (MAPE) between the results obtained with the detailed and equivalent models. The MAPEs in Fig. 3(a) and (d) are 0.36% and 0.11%, respectively. This is due to the small yet inevitable differences between the true and fitted $v_{OCV}-SoC$ curves in Supplementary Material A Fig. SA1.

Lastly, Fig. 3(d) shows the active power loss of the system P_{loss} . The observable trend with respect to SoC_0 is similar to that of \tilde{P}_{EV} . It is also worth pointing out that replacing EVs with constant PQ loads (horizontal gray line) would lead to a maximum over-estimation of the loss ΔP_{loss} (computed with respect to the case with $SoC_0=10\%$) of 1.84% for the LFP chemistry and 5.52% for the other ones when CCCV charging strategy is used. These errors increase with the penetration levels of EVs. This over-estimation is expected, since the adoption of constant PQ loads generally im-

plies consideration of a worst-case scenario [34].

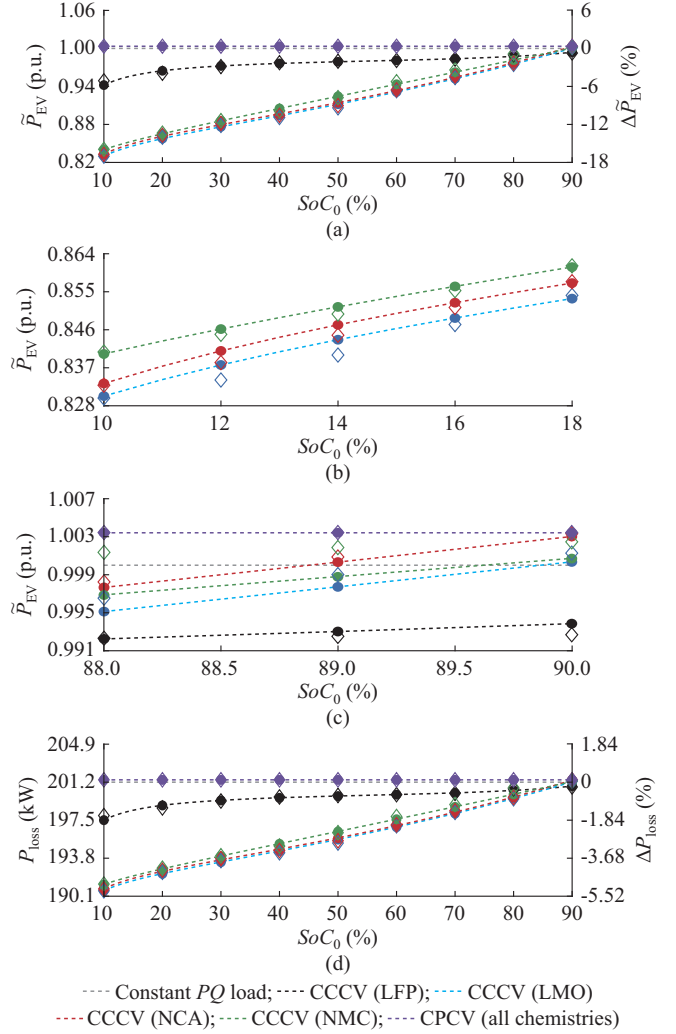


Fig. 3. Simulation results of modified feeder. (a) Active power exchange \tilde{P}_{EV} of a single EV (MAPE is 0.36%). (b) Inset of \tilde{P}_{EV} with SoC_0 of 10%-18%. (c) Inset of \tilde{P}_{EV} with SoC_0 of 88%-90%. (d) Active power loss P_{loss} in whole feeder (MAPE is 0.11%).

The above results show that, when CCCV charging strategy is considered, the cathode chemistry can make a difference in the results recorded during static grid studies (e.g., active power absorbed by EVs and losses). Disregarding this aspect (e.g., by replacing EVs with only constant PQ loads) would lead to mis-estimation of the true overload of the system induced by EVs, and, in turn, the losses. This estimation error is expected to increase with the penetration level of EVs scattered in the network.

Concerning computational costs, the CPU time to perform these simulations with PAN using the detailed EV model amounts to 174.4 s. On the contrary, when the proposed model is used, it is reduced to 105.2 s (i.e., a reduction of about 40%). In comparison, the CPU time to perform the simulation using constant PQ loads is 83.6 s (i.e., a reduction of 52%).

B. Dynamic Grid Studies of a Single EV

We consider again the K1 distribution feeder and focus on

the charging process of a single EV. At three different time instants during this process, we simulate a voltage step at the feeder substation to assess the capability of the model of capturing not only the evolution of SoC and power exchange but also its response after voltage disturbances.

Figure 4 shows the results of CCCV charging strategy of an EV with NMC cathode chemistry. The blue solid lines indicate the results obtained with the proposed model, while the red dashed lines with diamond markers refer to the detailed EV model. Figure 4(a), (c), and (e) shows the active power exchange \tilde{P}_{EV} , SoC, and the voltage magnitude \tilde{v} at the substation during the EV charging process (subject to three step changes of $\pm 15\%$), respectively. The comparison between the blue traces and red markers confirms again the accuracy of the proposed model. The MAPEs between the diamond markers and dashed lines in Fig. 4(a) and (c) are 1.54% and 0.02%, respectively, which are lower than 2%.

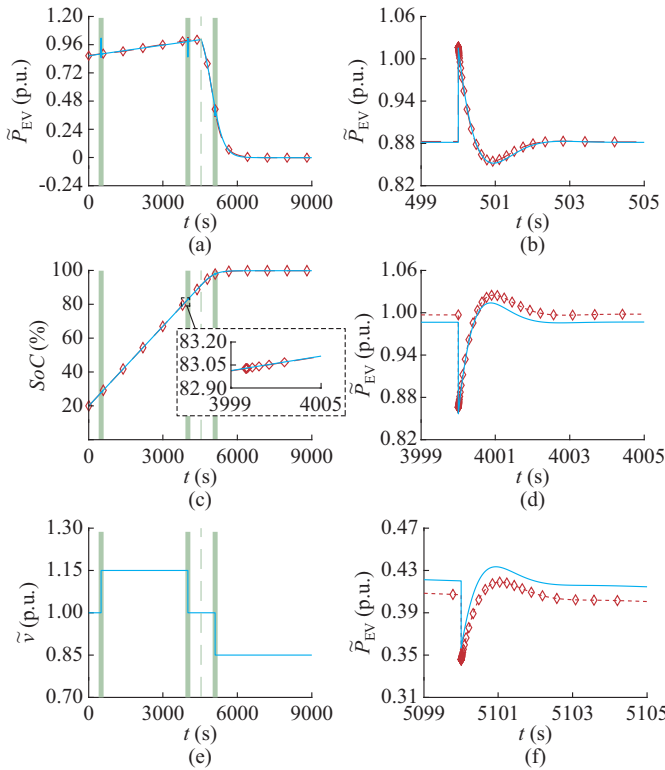


Fig. 4. Results of CCCV charging strategy of an EV with NMC cathode chemistry ($k_{p2}=0.6$, $k_{i2}=1$). (a) Active power exchange \tilde{P}_{EV} (MAPE is 1.54%). (b) Inset of \tilde{P}_{EV} from 499 to 505 s. (c) SoC (MAPE is 0.02%). (d) Inset of \tilde{P}_{EV} from 3999 to 4005 s. (e) Voltage magnitude \tilde{v} . (f) Inset of \tilde{P}_{EV} from $t=5099$ to 5105 s.

As to \tilde{P}_{EV} , the accuracy is better exemplified in Fig. 4(b), (d), and (f), which show \tilde{P}_{EV} around the three voltage steps (i.e., the green shaded areas in Fig. 4(a), (c) and (e)). Results show that the proposed model well replicates the behavior of the detailed one even if voltage disturbances have an amplitude quite different from that of a small signal (i.e., $\pm 15\%$). It is also worth noting that the last voltage disturbance occurs a long time after the PF solution is computed, to the extent that the charging mode might have shifted from CC/CP to CV (the time instants when this shift occurs are

denoted by green dashed vertical line). At this latter instance (i.e., Fig. 4(f)), one can notice that the black trace has a slight vertical offset with respect to the red markers. This difference is due to an inevitably imperfect fitting of the v_{OCV} -SoC relationship in the CV segment (i.e., SoC values close to 100%), which is reported in Supplementary Material A Fig. SA1.

Analogous comments can be made for Fig. 5, which shows similar results with the LMO cathode chemistry and CPCV charging strategy. In this case, the parameters k_{p2} and k_{i2} are set differently from how they are reported in Table III. Indeed, they are equal to 0.4 and 5, respectively. As can be observed from Figs. 4 and 5, it is reasonable to expect that the power response after voltage disturbances lasts for less than one minute, which is significantly less than the time needed for a full charging (i.e., SoC=100%). This justifies the second assumption put forward in Section III-C to build the small-signal model, which assumes that the SoC is constant for the whole duration of its response to voltage disturbances. This claim is also supported by the insets in Fig. 4(c) and Fig. 5(c), which shows the SoC right after a voltage disturbance.

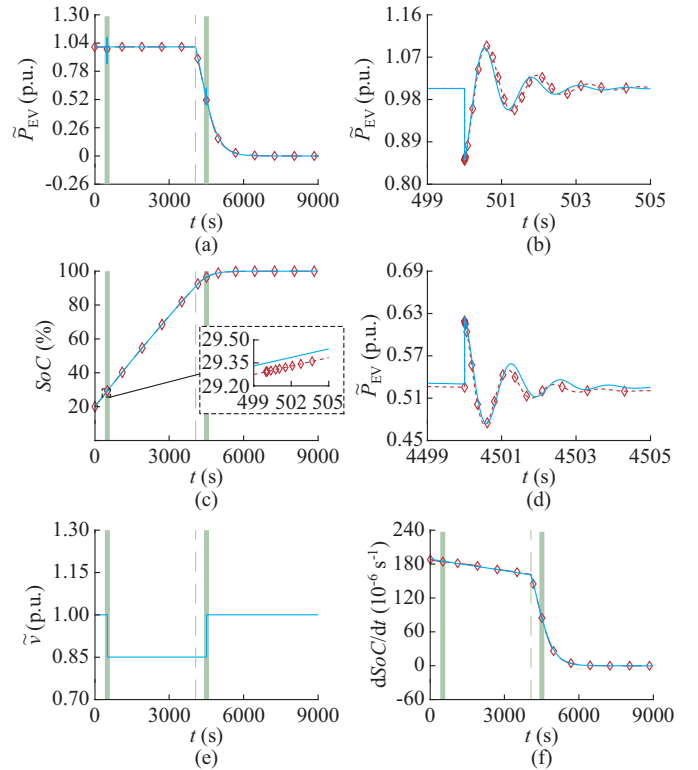


Fig. 5. Results of CPCV charging strategy of an EV with LMO cathode chemistry ($k_{p2}=0.4$, $k_{i2}=5$). (a) Active power exchange \tilde{P}_{EV} (MAPE is 1.61%). (b) Inset of \tilde{P}_{EV} from 499 to 505 s. (c) SoC (MAPE is 0.07%). (d) Inset of \tilde{P}_{EV} from 3999 to 4005 s. (e) Voltage magnitude \tilde{v} . (f) SoC derivative in whole charging process.

The CPU time needed to perform the full charging with the detailed EV model and proposed model amounts to 2.14 s and 0.71 s, respectively (i.e., a reduction of approximately 73%). These numbers are obtained by using a variable time step integration, with absolute and relative error tolerances on the electrical variables of 10^{-9} and 10^{-6} , respectively. If

fixed-time-step integration is to be used (as commonly done in commercial power system simulators), the CPU time would be much higher, but would anyway lean in favor of the adoption of the proposed model.

Additional simulation results can be found in Supplementary Materials C and D, which aim at comparing the proposed model when the LMO and NCA cathode chemistries are used, and showing how the cut-off frequency f_c of the LPFs is tuned.

C. Computational Efficiency of Proposed Model

We now pick as a benchmark the modified version of the IEEE 8500-bus system (please refer to Supplementary Material B). This large-scale system derives from a real distribution system in USA and is widely adopted in studies of smart grids and integration of distributed energy resources [35]. Here, we use it to further confirm the computational efficiency of the proposed model by adding several fleets of EVs, corresponding to the overload levels ranging from 0% to 100% with a step of 20%. It is worth mentioning that, when a 100% overload is considered, 240 EVs are connected (i.e., much more than the 28 EVs installed in the K1 distribution feeder). The numbers of equations required to simulate the system in this condition amount to 7.7×10^4 and 6×10^4 when the detailed EV model and the proposed model are used, respectively. On the contrary, when no EV is simulated, the number of equations is reduced to 4.3×10^4 .

For simplicity, EVs are assumed to have the same initial SoC with CCCV charging strategy and equipped with an LMO cathode chemistry. We modify the IEEE 8500-bus system by halving the nominal power of each load, including the EVs. This is necessary due to the limited power transmission capabilities of the system, which would have otherwise led to instability. For each overload level, we run two analyses on the simulator PAN. First, as in Section IV-A, we run a sequence of PF analyses by sweeping SoC_0 with a 1% step between 10% and 90%. Second, as in Section IV-B, we run an electromagnetic transient (EMT) analysis of about 3 hours to simulate the whole charging process (this is twice the time of 1.5 hours cited in Section III as the EV rated power is halved). Table IV shows the CPU time required with different overload levels by the detailed and proposed models to perform static and dynamic grid studies. The values inside parentheses have been obtained by exploiting circuit partitioning (refer to Supplementary Material E and [36]-[38] for further explanation) during simulation, while those without it have been obtained by running simulations as is.

As can be observed from the results of the static grid studies (i.e., middle columns), the reduction in CPU time granted by the proposed model ranges between 56% and 70% (i.e., when the overload level is 20% and 100%, respectively).

Concerning dynamic grid studies (i.e., rightmost columns), the CPU time for each model has been reported. When circuit partitioning is not exploited, the reduction of CPU time granted by the proposed model ranges between 16% and 28% (i.e., when the overload level is 20% and 100%, respectively). This range rises to 43% and 53% when circuit partitioning is exploited. As shown, the reduction of CPU time

granted by the proposed model is always evident, but it changes in each case depending on the techniques used to simulate the grid under analysis, which may vary in different power system simulators.

TABLE IV
CPU TIME REQUIRED WITH DIFFERENT OVERLOAD LEVELS

Overload level (%)	Number of EVs connected	CPU time needed to run a sequence of PF analyses (s)		CPU time needed to simulate whole charging process of 3 hours (s)	
		Detailed model	Proposed model	Detailed model	Proposed model
0	0	2.61	2.61	1.52	1.52
20	48	10.17	4.46	9.22 (1.90)	7.76 (1.08)
40	96	12.98	5.34	11.29 (3.88)	8.97 (1.79)
60	144	16.47	5.79	13.21 (6.16)	10.22 (2.82)
80	196	20.38	6.53	15.59 (8.56)	11.28 (3.95)
100	240	24.48	7.38	17.65 (10.63)	12.67 (4.98)

D. Dynamic Grid Studies of a Fleet of EVs

As a final test, we consider the IEEE 14-bus benchmark system (please refer to Supplementary Material B). We pick this benchmark system because, although its size is not excessively large, it allows connecting a reasonable number of distribution feeders with EVs to analyze the effect of EV mobility on the dynamic properties of the overall system. We modify the feeder by replacing the loads in the upper part of the grid with replicas of the K1 distribution feeder: for each replica, the rated power of the loads in the feeders (EVs included) is adjusted so that the overall power absorption matches that of the loads originally connected to the system. It is worth noting that this connection is possible without resorting to additional transformers because the nominal voltage of the upper part of the system coincides with that of the substation of the K1 distribution feeder (i.e., 13.8 kV).

We try to determine the maximum overload (contributed also by the $28 \times 7 = 196$ EVs scattered in the feeders) that can be applied before the occurrence of instability. To this aim, we increase the power rating of every load in the modified benchmark system (including those in the feeders and EVs) by a factor λ between 19% and 25% with a step of 0.1%. The power set-points of the slack and PV generators in the grid are adjusted accordingly. While doing so, we assume that for each EV, $SoC_0 = 10\%$, and that each EV adopts the LFP cathode chemistry and CPCV charging strategy. For each λ , we perform a PF analysis and an eigenvalue analysis (i.e., stability analysis) to detect when there is at least one eigenvalue with positive real part, which indicates an unstable system.

Figure 6(a) depicts how the maximum real part of the eigenvalues of the system σ_M evolves with λ . The colored lines (see the legend for details) correspond to the results obtained with different parameters of the PI controller that controls the DC-side voltage (i.e., PI_2 in Fig. 1(f)). We change these parameters as they are the only ones that appear in the transfer functions (13) and block ⑥ of Fig. 2. For each of the green, blue, and red traces, the solid lines and diamond markers are the results derived with the proposed and de-

tailed models, respectively. The fact that solid lines and markers superpose in each case confirms once again the accuracy of the proposed model, demonstrating that it is also suitable for stability analyses.

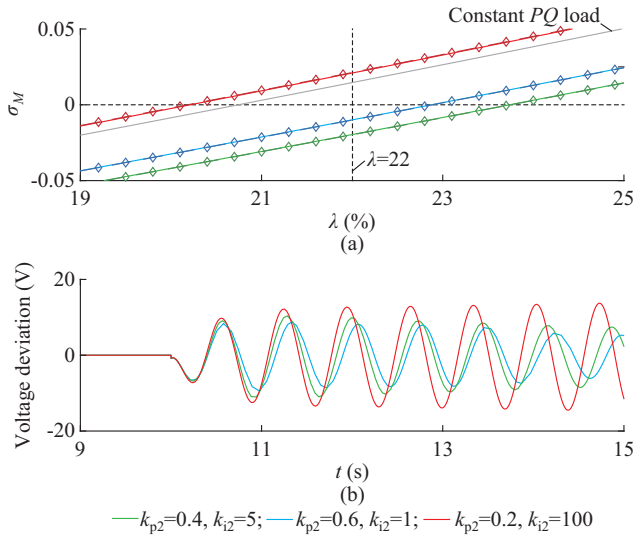


Fig. 6. σ_M and voltage deviations at bus 1 around its steady-state value due to a load disturbance. (a) σ_M by sweeping overload factor λ and adopting different values of k_{p2} and k_{i2} . (b) Voltage deviations at bus 1 with $\lambda=22\%$ and different values of k_{p2} and k_{i2} .

It is also worth noting that the value of λ leading to instability (i.e., $\sigma_M > 0$) varies with the PI control parameters. If all EVs are replaced by constant PQ loads (gray line), this threshold value would not be estimated correctly. For instance, by comparing the red and gray traces, instability is reached for lower values of λ in the former case. This refutes the claim that EV modeling as PQ loads always implies consideration of a worst-case scenario, and this is another reason why the proposed model might be useful. It is also worth adding that the CPU time needed to run these eigenvalue analyses with the proposed model is half that needed with the detailed model.

As a further proof of the results obtained with the eigenvalue analyses, we perform transient simulation of the modified IEEE 14-bus benchmark system by setting $\lambda=22\%$ and using the previous values of k_{p2} and k_{i2} . Based on the eigenvalue analysis and the above value of λ , the case with $k_{p2}=0.2$ and $k_{i2}=100$ (i.e., red trace) is unstable, whereas the other ones (i.e., blue and green traces) are stable. Indeed, for $\lambda=22\%$, $\sigma_M > 0$ only holds in the first case. This is confirmed by Fig. 6(b), which shows the voltage deviations at bus 1 around its steady-state value after a 10% step change at 10 s of load L_2 (refer to Supplementary Material B for its location). As expected, only when $k_{p2}=0.2$ and $k_{i2}=100$ are the voltage oscillations not damped, leading to the instability of the system. If CCCV charging strategy is considered, instability would occur for values of λ higher than those obtained with CPCV charging strategy. This happens because, for the same value of λ , the actual level of stress in the grid (e.g., higher currents and grid losses) due to the fleet of EVs is generally lower with CCCV charging strategy than with CPCV charging strategy, regardless of the value of SOC_0 . This feature, which can be

observed in Fig. 3, translates into higher stability margins.

V. DISCUSSION

The simulation shown in the previous section may lead us to ponder if similar results could have been attained with the other deterministic EV load models shown in Table I.

Concerning the simulation results in Section IV-A, they could have also been retrieved with comparable accuracy by using the multi-stage ZIP or exponential models presented in [12] and [14]. This holds if the SoC values considered in each stage are enough to fit the whole interval adopted, for instance, in Fig. 3. As stated in Section III-A, this requires storing a large enough look-up table where the ZIP or exponential load parameter values are saved for each SoC. Albeit not problematic from a computational standpoint, the proposed model follows a different approach and mirrors the EV behavior at steady state with a compact representation, i.e., (4) and (7).

On the contrary, the multi-stage ZIP models in [12] and [14] are not capable of providing the same results as the proposed model during the dynamic grid studies carried out in Sections IV-B, IV-C, and IV-D. In this context, the dynamic models developed in [16] and [17] lack the capability of updating the SoC over time. Updating this parameter is necessary because it changes the working condition of the EVs during the charging process, and consequently, the dynamic behaviors of EVs. For instance, if CCCV charging strategy is considered, we expect the EV power absorption to increase with SoC in the CC segment and decrease in the CV segment. Specifically, the model in [17] can yield results similar to the proposed model only if simulation is short enough and the SoC does not change significantly from the value at which the model derivation takes place. In addition, the model in [16] can only synthesize first-order dynamic responses.

VI. CONCLUSION

We propose an equivalent model of EVs with fast chargers for static and dynamic grid studies that is easy to implement, accurate, and computationally efficient. The proposed model is compatible with CCCV and CPCV charging strategies, as well as the most popular cathode chemistries adopted nowadays in the EV market. The proposed model can be used for both static and dynamic grid studies that involve a fleet of EVs. Contrary to the standard representation of EVs as constant PQ loads, the proposed model allows capturing how the active power of EVs varies with SoC during the regular charging process, as well as after voltage disturbances.

Specific application scenarios of the proposed model are examined in Section IV. The proposed model can be used to describe a fleet of EVs installed in large-scale feeders to perform PF analyses and determine how the increasing popularity of EV mobility affects voltage profiles, grid loading, and losses. In addition, the proposed model can be used in dynamic grid studies to assess how the charging process of a multitude of EVs interacts over time with already existing power system components after disturbances, and whether

stability issues might arise.

REFERENCES

- [1] IEA. (2023, Apr.). Global EV outlook 2023: catching up with climate ambitions. [Online]. Available: <https://www.iea.org/reports/global-ev-outlook-2023>
- [2] S. Habib, M. M. Khan, F. Abbas *et al.*, "A comprehensive study of implemented international standards, technical challenges, impacts and prospects for electric vehicles," *IEEE Access*, vol. 6, pp. 13866-13890, Mar. 2018.
- [3] A. Arias-Londoño, O. D. Montoya, and L. F. Grisales-Noreña, "A chronological literature review of electric vehicle interactions with power distribution systems," *Energies*, vol. 13, no. 11, p. 3016, Jun. 2020.
- [4] N. H. Tehrani and P. Wang, "Probabilistic estimation of plug-in electric vehicles charging load profile," *Electric Power Systems Research*, vol. 124, pp. 133-143, Jul. 2015.
- [5] J. C. Mukherjee and A. Gupta, "A review of charge scheduling of electric vehicles in smart grid," *IEEE Systems Journal*, vol. 9, no. 4, pp. 1541-1553, Dec. 2015.
- [6] A. Huaman-Rivera, R. Calloquispe-Huallpa, A. C. Luna Hernandez *et al.*, "An overview of electric vehicle load modeling strategies for grid integration studies," *Electronics*, vol. 13, no. 12, p. 2259, Jun. 2024.
- [7] Y. Amara-Ouali, Y. Goude, P. Massart *et al.*, "A review of electric vehicle load open data and models," *Energies*, vol. 14, no. 8, p. 2233, Apr. 2021.
- [8] A. M. A. Haidar and K. M. Muttaqi, "Behavioral characterization of electric vehicle charging loads in a distribution power grid through modeling of battery chargers," *IEEE Transactions on Industry Applications*, vol. 52, no. 1, pp. 483-492, Jan.-Feb. 2016.
- [9] J. Gil-Aguirre, S. Perez-Londono, and J. Mora-Flórez, "A measurement-based load modelling methodology for electric vehicle fast-charging stations," *Electric Power Systems Research*, vol. 176, p. 105934, Nov. 2019.
- [10] A. Visakh and M. P. Selvan, "Voltage dependent load models for EV chargers to improve the accuracy of grid-impact studies," in *Proceedings of 2022 International Virtual Conference on Power Engineering Computing and Control: Developments in Electric Vehicles and Energy Sector for Sustainable Future*, Chennai, India, May 2022, pp. 1-6.
- [11] A. M. A. Haidar, K. M. Muttaqi, and M. H. Haque, "Multistage time-variant electric vehicle load modelling for capturing accurate electric vehicle behaviour and electric vehicle impact on electricity distribution grids," *IET Generation, Transmission & Distribution*, vol. 9, no. 16, pp. 2705-2716, Dec. 2015.
- [12] E. Sortomme, A. I. Negash, S. S. Venkata *et al.*, "Voltage dependent load models of charging electric vehicles," in *Proceedings of 2013 IEEE PES General Meeting*, Vancouver, Canada, Jul. 2013, pp. 1-5.
- [13] C. H. Dharmakeerthi, N. Mithulananthan, and T. K. Saha, "Impact of electric vehicle fast charging on power system voltage stability," *International Journal of Electrical Power & Energy Systems*, vol. 57, pp. 241-249, May 2014.
- [14] A. Shukla, K. Verma, and R. Kumar, "Voltage-dependent modelling of fast charging electric vehicle load considering battery characteristics," *IET Electrical Systems in Transportation*, vol. 8, no. 4, pp. 221-230, Dec. 2018.
- [15] C. H. Dharmakeerthi, N. Mithulananthan, and A. Atputharajah, "Development of dynamic EV load model for power system oscillatory stability studies," in *Proceedings of 2014 Australasian Universities Power Engineering Conference*, Perth, Australia, Sept. 2014, pp. 1-6.
- [16] H. Tian, D. Tzelepis, and P. N. Papadopoulos, "Electric vehicle charger static and dynamic modelling for power system studies," *Energies*, vol. 14, no. 7, p. 1801, Apr. 2021.
- [17] H. Tian, E. O. Kontis, G. A. Barzegkar-Ntovom *et al.*, "Dynamic modeling of distribution networks hosting electric vehicles interconnected via fast and slow chargers," *International Journal of Electrical Power & Energy Systems*, vol. 157, p. 109811, Jun. 2024.
- [18] T. Ioannis, T. Dalius, and L. Natalia. (2018, Nov.). Li-ion batteries for mobility and stationary storage applications. [Online]. Available: <http://publications.jrc.ec.europa.eu/repository/bitstream/JRC113360/kjna29440enn.pdf>
- [19] P. H. Camargos, P. H. J. dos Santos, I. R. dos Santos *et al.*, "Perspectives on Li-ion battery categories for electric vehicle applications: a review of state of the art," *International Journal of Energy Research*, vol. 46, no. 13, pp. 19258-19268, Oct. 2022.
- [20] B. Barać, M. Krpan, T. Capuder *et al.*, "Modeling and initialization of a virtual synchronous machine for power system fundamental frequency simulations," *IEEE Access*, vol. 9, pp. 160116-160134, Nov. 2021.
- [21] M. Restrepo, J. Morris, M. Kazerani *et al.*, "Modeling and testing of a bidirectional smart charger for distribution system EV integration," *IEEE Transactions on Smart Grid*, vol. 9, no. 1, pp. 152-162, Jan. 2018.
- [22] G. L. Plett, *Battery Management Systems, Volume I: Battery Modeling*. Norwood: Artech House, 2015.
- [23] M. K. Tran, A. Costa, A. Mevawalla *et al.*, "Comparative study of equivalent circuit models performance in four common lithium-ion batteries: LFP, NMC, LMO, NCA," *Batteries*, vol. 7, no. 3, p. 51, Sept. 2021.
- [24] A. Yazdani and R. Iravani, *Voltage-sourced Converters in Power Systems: Modeling, Control, and Applications*. Hoboken: John Wiley & Sons, 2010.
- [25] J. A. Sanguesa, V. Torres-Sanz, P. Garrido *et al.*, "A review on electric vehicles: technologies and challenges," *Smart Cities*, vol. 4, no. 1, pp. 372-404, Mar. 2021.
- [26] O. Tremblay and L. A. Dessaint, "Experimental validation of a battery dynamic model for EV applications," *World Electric Vehicle Journal*, vol. 3, no. 2, pp. 289-298, Jun. 2009.
- [27] The MathWorks Inc. (2022, Dec.). Simulation and model-based design (Simulink). [Online]. Available: <https://ww2.mathworks.cn/en/products/simulink.html>
- [28] D. del Giudice. (2024, Nov.). Electric vehicle models. [Online]. Available: https://github.com/Davide-del-Giudice/Electric_vehicle_models.git
- [29] F. Postigo Marcos, C. Mateo Domingo, T. Gómez San Román *et al.*, "A review of power distribution test feeders in the United States and the need for synthetic representative networks," *Energies*, vol. 10, no. 11, p. 1896, Nov. 2017.
- [30] D. Linaro, D. del Giudice, F. Bizzarri *et al.*, "PanSuite: a free simulation environment for the analysis of hybrid electrical power systems," *Electric Power Systems Research*, vol. 212, p. 108354, Nov. 2022.
- [31] F. Bizzarri and A. Brambilla, "PAN and MPanSuite: simulation vehicles towards the analysis and design of heterogeneous mixed electrical systems," in *Proceedings of 2017 New Generation of CAS*, Genova, Italy, Sept. 2017, pp. 1-4.
- [32] F. Bizzarri, A. Brambilla, G. S. Gajani *et al.*, "Simulation of real world circuits: extending conventional analysis methods to circuits described by heterogeneous languages," *IEEE Circuits and Systems Magazine*, vol. 14, no. 4, pp. 51-70, Fourthquarter2014.
- [33] D. Montenegro, M. Hernandez, and G. A. Ramos, "Real time OpenDSS framework for distribution systems simulation and analysis," in *Proceedings of 2012 Sixth IEEE/PES Transmission and Distribution: Latin America Conference and Exposition*, Montevideo, Uruguay, Sept. 2012, pp. 1-5.
- [34] D. del Giudice, F. Bizzarri, S. Grillo *et al.*, "Impact of passive-components' models on the stability assessment of inverter-dominated power grids," *Energies*, vol. 15, no. 17, p. 6348, Sept. 2022.
- [35] R. F. Arritt and R. C. Dugan, "The IEEE 8500-node test feeder," in *Proceedings of IEEE/PES Transmission and Distribution (T&D) Conference and Exposition*, New Orleans, USA, Nov 2010, pp. 1-6.
- [36] A. Sangiovanni-Vincentelli, L. Chen, and L. Chua, "An efficient heuristic cluster algorithm for tearing large-scale networks," *IEEE Transactions on Circuits and Systems*, vol. 24, no. 12, pp. 709-717, Dec. 1977.
- [37] L. Nagel, "SPICE2: a computer program to simulate semiconductor circuits," University of California, Berkeley, USA, Tech. Rep. UCB/ERL M520, 1975.
- [38] K. Sun, Q. Zhou, K. Mohanram *et al.*, "Parallel domain decomposition for simulation of large-scale power grids," in *Proceedings of 2007 IEEE/ACM International Conference on Computer-Aided Design*, San Jose, USA, Nov. 2007, pp. 54-59.

Davide del Giudice received the M.S. degree (cum laude) and Ph.D. degree (cum laude) in electrical engineering from Politecnico di Milano, Milano, Italy, in 2017 and 2022, respectively. He is currently a Researcher with the Department of Electronics, Information and Bioengineering, Politecnico di Milano. His main research interests include simulation technique for electric power system with high penetration of converter-interfaced elements such as high-voltage direct current system, electric vehicle, and generation fuelled by renewable energy.

Angelo Maurizio Brambilla received the Dr.Ing. degree in electronic engineering from University of Pavia, Pavia, Italy, in 1986. He is a Full Professor with the Department of Electronics, Information and Bioengineering, Po-

litenico di Milano, Milano, Italy. His research interests include circuit analysis, simulation, and modeling.

Federico Bizzarri received the Laurea (M.Sc.) degree (summa cum laude) in electronic engineering and the Ph.D. degree in electrical engineering from University of Genoa, Genoa, Italy, in 1998 and 2001, respectively. Since October 2018, he has been an Associate Professor with the Politecnico di Milano, Milano, Italy. He is a Research Fellow of the Advanced Research Center on Electronic Systems for Information and Communication Technologies “E. De Castro” (ARCES), University of Bologna, Bologna, Italy. His main research interests include nonlinear circuit, with emphasis on chaotic dynamics and bifurcation theory, circuit model of nonlinear system, image processing, circuit theory, and simulation.

Daniele Linaro received the M.Sc. degree in electronic engineering and the Ph.D. degree in electrical engineering from University of Genoa, Genoa, Ita-

ly, in 2007 and 2011, respectively. Since 2025, he has been an Associate Professor with the Department of Electronics, Information Technology and Bioengineering, Politecnico di Milano, Milano, Italy. His main research interests include circuit theory and nonlinear dynamical system, with application to electronic oscillator and power system and computational neuroscience, in particular biophysically realistic single-cell model of neuronal cells.

Samuele Grillo received the Laurea (M.Sc.) degree in electronic engineering, and the Ph.D. degree in power systems from the University of Genoa, Genoa, Italy, in 2004 and 2008, respectively. He is currently an Associate Professor with the Department of Electronics, Information Technology and Bioengineering, Politecnico di Milano, Milano, Italy. His research interests include smart grid, integration of distributed renewable sources and energy storage devices in power systems, and optimization and control techniques applied to power systems.